GEOPHYSICS, VOL. 83, NO. 2 (MARCH-APRIL 2018); P. JM1–JM14, 8 FIGS., 2 TABLES.
10.1190/GEO2016-0574.1

Numerically optimized modulations for adiabatic pulses in surface nuclear magnetic resonance

Denys Grombacher[1]

ABSTRACT

Adiabatic pulses, which provide an effective means of generating a large-amplitude nuclear magnetic resonance (NMR) signal in the presence of a heterogeneous magnetic field, have the potential to greatly improve the signal-to-noise ratio of the surface NMR experiment. To ensure efficient implementation of adiabatic pulses into the surface NMR framework, a numerically optimized modulation (NOM) approach is used to design adiabatic pulses specifically intended for application in surface NMR. The scenario in which the frequency response of the tuned transmit coil is used to modulate the current amplitude is considered. The performance of a NOM pulse is contrasted against two alternative adiabatic pulses (described by a linear frequency sweep and a hyperbolic tangent sweep) that are currently implemented with the existing hardware. The NOM approach provides equivalent excitation as the chirp and hyperbolic tangent pulse while shortening pulse durations and reducing power consumption. Furthermore, the NOM approach also provides sharp resolution and large signal amplitudes. Considerations for the design of the NOM adiabatic pulse for surface NMR are given, as well as a discussion about their implementation into the surface NMR experimental framework.

INTRODUCTION

Surface nuclear magnetic resonance (NMR) is a noninvasive geophysical technique providing insight into subsurface water content (Legchenko and Valla, 2002) and pore-scale properties such as pore size and permeability (Mohnke and Yaramanci, 2008). One challenge commonly confronted in surface NMR is a low signal-to-noise ratio (S/N) (Legchenko, 2007; Walsh, 2008). This is partly a consequence of using the earth's magnetic field as the background magnetic field B_0 in surface NMR. The strength of the magnetization measured in an NMR experiment scales with the amplitude of the background magnetic field (Halse and Callaghan, 2008; Levitt, 2008); this is the reason that the vast majority of NMR experiments are conducted using strong magnets with elevated B_0. As a result, the magnetization measured by surface NMR is very small. Combined with this challenge is the difficulty that the surface NMR signal exists in a frequency band (at approximately 2 kHz) in which the noise floor is often much larger than the NMR signal (Dalgaard et al., 2012; Müller-Petke and Costabel, 2014). These factors often result in a low S/N in surface NMR.

Two approaches have been used to improve the S/N in surface NMR. The first is the development of strategies to reduce the noise level. This approach has seen much success, from the development of reference coil techniques (Walsh, 2008; Dalgaard et al., 2012; Müller-Petke and Costabel, 2014), and model-based subtraction methods to eliminate the influence of power line harmonics (Larsen et al., 2014), to approaches that deal with high-amplitude, short-duration "spike" noise due to sferics and electric fences (Costabel and Müller-Petke, 2014; Larsen, 2016). Another approach to reduce the noise level is to use a figure-eight receive coil (Trushkin et al., 1994), which has inherent noise cancellation properties. These techniques have greatly expanded the range of conditions in which the surface NMR experiment can be conducted (Müller-Petke and Costabel, 2013), but low S/N remains a common challenge.

Another approach to improve S/N is to develop a transmit strategy capable of directly improving the signal quality. Several studies have implemented alternative transmit strategies differing from the standard free-induction decay (FID) measurement, such as pseudosaturation (Legchenko et al., 2004; Walbrecker et al., 2011), spin-echo (Shushakov, 1996; Legchenko et al., 2010; Grunewald et al., 2014), and multiecho (Grunewald and Walsh, 2013a) pulse sequences. These techniques focus on improving the information content of the measured relaxation times, parameters that describe the signal's decay. In a strongly heterogeneous B_0 field, the spin-echo and multiecho can also produce a measureable signal in some situations

Manuscript received by the Editor 9 November 2016; revised manuscript received 15 September 2017; published ahead of production 11 November 2017; published online 28 December 2017.
[1]Aarhus University, Hydrogeophysics Group, Geoscience Department, Aarhus, Denmark. E-mail: denys.grombacher@geo.au.dk.

in which an FID could not (Legchenko et al., 2010) because the FID signal may have decayed fully before the start of the measurement. Spin-echo and multiecho approaches can also extend the duration of the surface NMR signal compared with the FID, which can lead to S/N improvements in certain cases. Other transmit approaches have been shown to improve the spatial resolution of surface NMR images by transmitting off-resonance or by using a composite pulse (Grombacher et al., 2014). Off-resonance excitation has also been shown to reduce modeling errors related to background magnetic field inhomogeneity via the frequency-cycling approach (Grombacher et al., 2016). Each of these alternative transmit strategies is capable of improving survey performance, but do not focus primarily on increasing S/N; one of the major challenges in surface NMR. To address this concern directly, Grunewald et al. (2016) implement an adiabatic pulse to enhance the signal amplitude and observe an S/N improvement by a factor of approximately 3. Using an adiabatic pulse to improve the measurement S/N differs from noise cancellation approaches in that it directly enhances the signal amplitude instead of reducing the noise level.

Adiabatic pulses differ from the on-resonance pulse typically used in surface NMR because the oscillation frequency of the current in the transmit coil (the transmit frequency, ω_t) varies throughout the pulse. In contrast, ω_t is constant during an on-resonance pulse (also during approaches using an off-resonance pulse). As

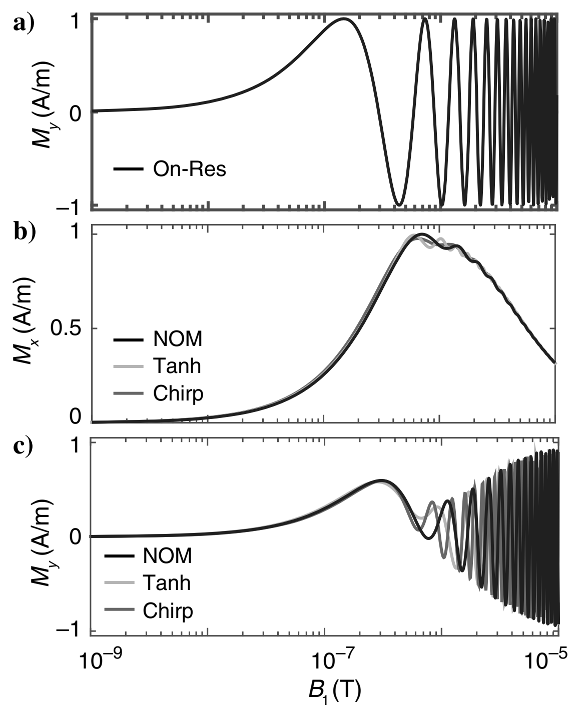

Figure 1. (a) The M_y component produced by a 40 ms on-resonance pulse over a range of B_1. (b and c) The M_x and M_y components, respectively, expected following several example adiabatic pulses for a range of B_1 amplitudes. The black, dark-gray, and light-gray lines correspond to an example NOM, chirp, and hyperbolic tangent pulse, respectively. The NOM pulse is determined by $A/2\pi = 100$ Hz, $\nu = [1 \quad 2]$, $\gamma_0 = 10$, and $B/\gamma = 1\mathrm{e}-6\ T$. The chirp pulse is described by a linear frequency sweep of $A/2\pi = 100$ Hz and $\tau = 100$ ms. The hyperbolic tangent sweep is defined by $A/2\pi = 100$ Hz, $\tau = 40$ ms, and $\eta = 1.5$. In each case $Q = 10$, and the amplitude modulation is coupled to the instantaneous transmit frequency via the coil response.

a result, the net perturbation of the magnetization is different during an adiabatic pulse compared with an on-resonance pulse. This difference gives adiabatic pulses several attractive features, such as their ability to improve performance in a heterogeneous applied magnetic field (B_1) (Ugurbil et al., 1987; Garwood and Ke, 1991), like that present in surface NMR. To exploit this feature in surface NMR, an adiabatic pulse called an adiabatic half-passage (AHP) (Tannus and Garwood, 1997; Garwood and Delabarre, 2001) may be used as the excitation pulse in an FID experiment (Grunewald et al., 2016). This type of pulse can be designed to mitigate the effects of B_1 heterogeneity due to hardware imperfections (Bendall and Pegg, 1986) and to provide precise performance in the presence of a B_0 gradient to improve imaging capabilities (Silver et al., 1984). Adiabatic pulses can also be designed to serve as inversion pulses insensitive to B_1 or B_0 inhomogeneity (Baum et al., 1985) or as refocusing pulses, (Conolly et al., 1989) but in this case we focus on their ability to function as an excitation pulse given that our goal is to improve the S/N for FID experiments.

We aim to design adiabatic pulses specifically intended for implementation in surface NMR conditions. A numerically optimized modulation (NOM) approach (Ugurbil et al., 1988; Town and Rosenfeld, 1990; Skinner and Robitaille, 1992) is implemented to design efficient frequency sweeps for adiabatic pulses given conditions representative of surface NMR. We consider the scenario in which the current amplitude is coupled to the instantaneous transmit frequency via the transmit coil's frequency response. This scenario simplifies the design of the adiabatic pulse, requiring only the frequency sweep to be specified. Previous implementations of adiabatic pulses in surface NMR have also used the coil response to modulate the current amplitude (Grunewald et al., 2016). Advantages of the NOM approach are illustrated through synthetic comparison with a chirp adiabatic pulse (where the transmit frequency is varied linearly with time) and a hyperbolic tangent adiabatic pulse (where the transmit frequency is varied using a hyperbolic tangent function), which represent the two adiabatic pulses currently implemented in the surface NMR instrumentation. Feasibility of the NOM pulse is also demonstrated in a field experiment. Discussion about implementation of the adiabatic pulse into the surface NMR framework is given, and the ability of adiabatic pulses to produce high-resolution images is investigated.

BACKGROUND

Surface NMR excitation pulses

To generate a measureable signal in surface NMR, the magnetization present in the subsurface must be given a component transverse to Earth's field. This is accomplished by perturbing the magnetization out of its equilibrium along the earth's field direction using an applied magnetic field (B_1). The standard excitation pulse in surface NMR is an on-resonance pulse (Legchenko and Valla, 2002; Behroozmand et al., 2015); it is called on-resonance because the transmit frequency (ω_t) is selected equal to the Larmor frequency (ω_0), resulting in an offset ($\Delta\omega$) equal to zero during the pulse. The B_1 amplitude is also constant during an on-resonance pulse. Figure 1a illustrates the transverse magnetization produced by a 40 ms on-resonance pulse over a broad range of B_1 typical of that present in surface NMR. Each point in the profile is formed by solving the Bloch equation (Bloch, 1946) given the 40 ms on-resonance pulse waveform, a single B_1 amplitude, and an initial condition described by a unit magnetization at equilibrium. A transverse component (x- or y-component) equal to one indicates that the pulse will rotate the magnetization fully into the transverse plane given that particular B_1 magnitude, whereas values close to zero indicate that the magnetization remains in the earth's field direction. At a small B_1 in Figure 1a, the transverse component is close to zero. Moving to a larger B_1, the profile rises to form a peak with amplitude one and then begins to oscillate rapidly between positive and negative values at large B_1. Positive and negative values correspond to transverse magnetizations oriented in opposite directions. The rapid oscillation results from the large induced flip angles at these B_1 strengths for the on-resonance pulse. Note that the positive and negative values will lead to destructive interference that reduces the net signal amplitude. To eliminate this destructive interference and ultimately increase the signal amplitude, Grunewald et al. (2016) propose that an alternative excitation strategy using an adiabatic pulse may be used.

The type of adiabatic pulse used to generate a transverse magnetization is called an AHP pulse (Tannus and Garwood, 1997). An AHP pulse begins with a large offset, sweeps ω_t toward ω_0 during the pulse, and ends when the offset is equal to zero. Figure 1b and 1c illustrates the transverse components produced by three example AHP pulses; Figure 1b and 1c illustrates the x- and y-components of the transverse magnetization, respectively. The transverse components are determined in the same manner as in Figure 1a, except with a pulse waveform corresponding to the appropriate AHP. Note that only the y-component is shown for the on-resonance case because its x-component is equal to zero at all B_1 (not shown). The details of the three example adiabatic pulses are given in the following section. For now, they serve to illustrate several examples of the performance of an AHP pulse in a heterogeneous B_1. The x-profiles (Figure 1b) are described by a single broad peak with only positive values. The broad peak is a consequence of AHP pulses exhibiting reduced sensitivity to B_1 heterogeneity (Ugurbil et al., 1987). For the y-component (Figure 1c), the profiles are described by an initial bump, followed by strong oscillatory behavior at large B_1. Note that the oscillation in the M_y profiles is not due to modeling instability; rather, it is a consequence of the initial condition not being well-satisfied at a large B_1 given the initial offsets. The presence of a nonzero y-component is a consequence of these example AHP pulses not perfectly satisfying the conditions required for an AHP at all B_1. Further discussion about the features observed in Figure 1c is given in the following section.

The motivation to use an AHP pulse in surface NMR stems from a desire to exploit the broad positive peak in Figure 1b. The broad peak indicates that significant transverse components can be produced over a wide B_1 range and consistently with a positive x-component (which would eliminate destructive interference). Grunewald et al. (2016) demonstrate that an AHP can lead to significant signal improvements in surface NMR, but questions remain about which AHP pulses are best suited to surface NMR conditions.

Designing an AHP pulse

To help understand the perturbation of the magnetization during an AHP it is convenient to define a vector $\boldsymbol{\omega}_{\text{eff}}$ equal to

$$\boldsymbol{\omega}_{\text{eff}} = \begin{bmatrix} \omega_1 \\ 0 \\ \Delta\omega \end{bmatrix}, \tag{1}$$

where ω_1 is equal to $\gamma * B_1$ (γ is the gyromagnetic ratio of the hydrogen nuclei). The $\Delta\omega$ term describes the offset between the Larmor frequency and the transmit frequency; $\Delta\omega = \omega_0 - \omega_t$. Equation 1 is valid in a reference frame that rotates at the transmit frequency and has the z- and x-axes oriented in the direction of the earth's field and the direction of the component of B_1 perpendicular to the earth's field, respectively.

For a particular excitation pulse to be considered as an AHP pulse, it must satisfy three conditions. The first requires that the transmit frequency at the beginning of the pulse be selected such that $\Delta\omega \gg \omega_1$. This ensures that $\boldsymbol{\omega}_{\text{eff}}$ is effectively collinear with the equilibrium orientation of the magnetization at the onset of the pulse. Note that if this condition ($\Delta\omega \gg \omega_1$) is not well-satisfied, it leads to behavior similar to that observed in Figure 1c (strong oscillations in the M_y component). The second requirement is that the AHP pulse ends when $\boldsymbol{\omega}_{\text{eff}}$ is in the transverse plane (satisfied by ending the pulse when $\Delta\omega = 0$). The third requirement is that the frequency sweep satisfy the adiabatic condition at all times; i.e., $\Gamma \gg 1$, where Γ is the adiabaticity factor defined by

$$\Gamma(\omega_0, t) = \frac{\|\boldsymbol{\omega}_{\text{eff}}(\omega_0, t)\|}{|\dot{\theta}(\omega_0, t)|}. \tag{2}$$

The time derivative of the angle θ describes the change in the $\boldsymbol{\omega}_{\text{eff}}$ axis' orientation, where $\tan(\theta) = \Delta\omega/\omega_{\mathbf{1}}$. The adiabatic condition is satisfied well when the nutation frequency $\boldsymbol{\omega}_{\text{eff}}$ is much greater than the rate of change for the $\boldsymbol{\omega}_{\text{eff}}$ axis' orientation. If all three conditions are well-satisfied the magnetization will remain locked to the $\boldsymbol{\omega}_{\text{eff}}$ vector throughout the AHP pulse, ultimately ending the pulse with an orientation that lies in the transverse plane; that is, the AHP pulse effectively functions as a $\pi/2$ pulse.

In principle, we have the freedom to modulate the current amplitude during the pulse (i.e., ω_1) and ω_t separately. Pulse-width modulation may be used to directly modulate the current amplitude during the pulse. This allows independent manipulation of $\omega_1(t)$ and $\Delta\omega(t)$ giving precise control over the orientation of the $\boldsymbol{\omega}_{\text{eff}}$ vector. Alternatively, previous implementations of adiabatic pulses in surface NMR have used the transmit coil's frequency response to modulate the current amplitude. In this scenario, $\omega_1(t)$ is coupled to $\Delta\omega(t)$ via the frequency response of the tuned transmit coil. We consider the case in which the coil response is used to modulate the current amplitude; this approach simplifies the design of an adiabatic pulse to specifying only $\Delta\omega(t)$. In this study, we model the coil response as a Lorentzian, where the Lorentzian is centered at ω_0 and has a width determined by the transmit coil quality factor Q (the equation defining the relation between $\Delta\omega$ and ω_1 is given in equation A-1).

In the following, we investigate the utility of three types of frequency sweeps: (1) a linear frequency sweep (referred to as a chirp pulse), (2) a hyperbolic tangent frequency sweep, and (3) a frequency sweep defined by a NOM (referred to as a NOM pulse). Grunewald et al. (2016) implement a chirp pulse and observe promising results. A frequency sweep described by a hyperbolic tangent function has also been implemented in the Vista Clara GMR surface NMR data acquisition software. For these two example sweeps, $\Delta\omega(t)$ are given by

$$\Delta\omega_c(t) = A\left(1 - \frac{t}{\tau}\right), \tag{3a}$$

and

$$\Delta\omega_{\mathrm{ht}}(t) = A\left(1 - \frac{\tanh(\frac{\eta t}{\tau})}{\tanh(\eta)}\right). \tag{3b}$$

Equation 3a and 3b corresponds to the frequency sweeps for the chirp pulse and hyperbolic tangent cases, respectively. Subscripts of c and ht will be used to denote chirp and hyperbolic tangent sweeps. Equation 3a and 3b is parameterized such that $\Delta\omega(t=0) = A$ and $\Delta\omega(t=\tau) = 0$, where A is the initial offset and τ is the sweep duration. For the hyperbolic tangent sweep, the η parameter controls the shape of $\Delta\omega_{\mathrm{ht}}(t)$. Large η values produce $\Delta\omega_{\mathrm{ht}}(t)$ that sweep rapidly at the beginning of the pulse but slow as $\Delta\omega_{\mathrm{ht}}(t)$ approaches zero. In the small η limit, the hyperbolic tangent sweep approaches a linear frequency sweep.

For the NOM approach (Ugurbil et al., 1988), the frequency sweep is determined using an optimization that ensures that a minimum Γ is maintained throughout the pulse over a specified B_1 range. The advantage of the NOM approach is that it implicitly balances a desire to produce the fastest possible sweep (to reduce power requirements and minimize relaxation during pulse [RDP] effects [Walbrecker et al., 2009]) with the need to ensure a minimum level of adiabaticity is maintained. The NOM method and how it is used to determine the frequency sweep $\Delta\omega(t)$ is described in detail by Rosenfeld et al. (1997). Briefly, given fixed shapes of the $\Delta\omega(t)$ and $\omega_1(t)$ functions, the NOM approach can be used to determine the optimal timing of the frequency sweep that ensures a minimum Γ is maintained over a specific B_1 range throughout the pulse. The duration of the NOM sweep is determined during the optimization. The optimization is given the freedom to sweep as quickly or as slowly as needed to satisfy the minimum adiabaticity requirement. The final shape of a particular NOM sweep is controlled by several parameters: B, ν, γ_0, and A. The B_1 range in which the minimum adiabaticity requirement must be satisfied is determined by B and ν, where B is used to specify a target B_1 and ν is used to scale this value to cover the B_1 range of interest. The selection of B and ν to describe a B_1 range is not unique. The γ_0 parameter specifies the minimum adiabaticity factor that must be maintained over the specified B_1 range during the pulse; A is the initial offset between the transmit and Larmor frequencies. The coil factor Q must also be specified prior to the optimization because it enters ω_1 through the coil response. Further details about the implementation of the NOM approach for the scenario in which ω_1 is coupled to the instantaneous $\Delta\omega$ are given in Appendix A.

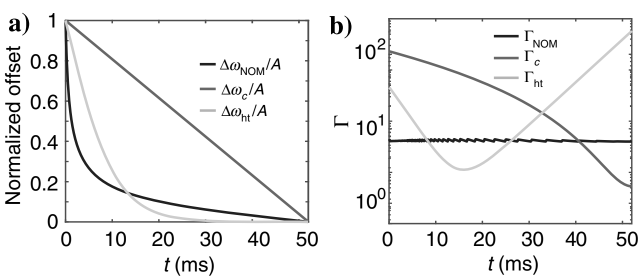

Figure 2. (a) Schematic illustrating the modulation of the transmit frequency during three example adiabatic pulses. The black line shows the variation of the transmit frequency for a NOM pulse corresponding to $A/2\pi = 100$ Hz, $B/\gamma = 3\mathrm{e}-7\ T$, $\gamma_0 = 4$, $\nu = 1$, and $Q = 10$. The dark-gray line shows the variation of the transmit frequency for a chirp pulse (linear frequency sweep) with to the same A and pulse duration (52.2 ms) as the NOM pulse. The light-gray line shows the variation of the transmit frequency for a hyperbolic tangent sweep with $\eta = 4$ and the same A and pulse duration as the NOM pulse. (b) The adiabaticity factor throughout the adiabatic pulse for each of the adiabatic pulses shown in (a) for a $B_1 = 3\mathrm{e}-7\ T$.

To contrast the characteristics of the three investigated types of frequency sweeps, Figure 2a compares the shapes of example chirp, hyperbolic tangent, and NOM $\Delta\omega(t)$ functions with equal durations ($\tau = 52.2$ ms), starting offset A ($A/2\pi = 100$ Hz), and coil response ($Q = 10$ and $f_0 = 2000$ Hz). Figure 2b illustrates the adiabaticity factor for a B_1 of $3\mathrm{e}-7\ T$ during each of the sweeps shown in Figure 2a. In practice, the surface NMR measurement has an extremely heterogeneous B_1, but a single value is considered in Figure 2b to simplify a qualitative discussion about the differences among the NOM, chirp, and hyperbolic tangent sweeps. The value of B_1 used in this example is chosen to correspond to the target B_1 for the example NOM pulse. Figure 2a illustrates $\Delta\omega_{\mathrm{NOM}}(t)$, for a sweep with $B/\gamma = 3\mathrm{e}-7\ T$, $\gamma_0 = 4$, and $\nu = 1$, as the black line. The $\Delta\omega_{\mathrm{c}}(t)$ function corresponding to the example chirp pulse is shown by the dark-gray line. The $\Delta\omega_{\mathrm{ht}}(t)$ function corresponding to the example hyperbolic tangent sweep with $\eta = 4$ is shown by the light-gray line. In each case, $\omega_1(t)$ (not shown) is determined by the coil response.

For the NOM sweep (black line in Figure 2a), the transmit frequency is initially swept quickly with the sweep rate slowing as $\Delta\omega$ approaches zero. This can be seen by noting that the slope is initially steep but flattens toward the end of the pulse. The exact shape of the sweep depends on the selection of the A, B, γ_0, and ν parameters, but the NOM sweeps typically exhibit a shape similar to that shown in Figure 2a. The changing slope of the NOM frequency sweep results from the minimum adiabaticity requirement. This can be observed in Figure 2b, which illustrates the adiabaticity factor throughout the pulse at the target B_1 of $3\mathrm{e}-7\ T$. The NOM pulse sweeps as fast as possible while satisfying the minimum adiabaticity requirement resulting in a flat response in Figure 2b. Note that Γ during the NOM pulse is only constant over the B_1 range in which the minimum adiabaticity requirement is enforced, at other B_1 Γ varies during the pulse. For the chirp pulse example (the dark-gray line in Figure 2a), ω_t is varied at a constant rate throughout the pulse (corresponding to the constant slope). Compared with the NOM sweep, the chirp pulse sweeps more slowly initially and more quickly toward the end of the pulse. The adiabaticity factor throughout the chirp pulse (the dark-gray line in Figure 2b) is initially large, but it decreases toward the end of the pulse (for $B_1 = 3\mathrm{e}-7\ T$). For the hyperbolic tangent sweep (light gray line in Figure 2a), the shape is closer to the NOM case except that the initial sweep and the approach to resonance are slower (the slope is flatter during the latter half of the pulse). The exact shape of the hyperbolic tangent sweep is controlled by η, but it generally exhibits a similar shape to that shown in Figure 2a. Examining the adiabaticity factor during the hyperbolic tangent sweep indicates that it begins with a high Γ, which dips to a lower Γ at times corresponding to the shoulder in Figure 2a (i.e., $t \sim 15$ ms in this example). At later times, the slow approach to resonance produces a high Γ (for $B_1 = 3\mathrm{e}-7\ T$). However, adiabaticity considerations alone (e.g., Figure 2b) are not enough to comment on the expected relative performance of each frequency sweep.

RESULTS

Numerical comparison of chirp, hyperbolic tangent, and NOM AHP pulses for surface NMR conditions

The suitability of an adiabatic pulse for surface NMR must also be judged by several additional factors such as

1) its ability to generate a transverse magnetization in the presence of a heterogeneous B_1,
2) the pulse duration,
3) the power requirement, and
4) its utility for producing high-resolution images of aquifer properties.

The first factor is related to the pulse's ability to generate a large amplitude signal given heterogeneous B_1. The second factor considers the impact of RDP effects (Walbrecker et al., 2009), which places an upper limit on the pulse duration. The third factor is a practical consideration related to hardware limitations, and the fourth factor reflects that, ultimately, the goal in surface NMR is to produce images of aquifer properties. Therefore, the performance of a pulse must be judged not only by its ability to generate a large transverse magnetization but also how useful it is for the imaging portion of the problem. In the following, we contrast the chirp, hyperbolic tangent, and NOM frequency sweeps based on these four criteria.

Consider first the ability of each type of sweep to produce a transverse magnetization in a heterogeneous B_1 (factor 1). In Figure 1b and 1c, the M_x and M_y components for three example adiabatic pulses are illustrated: a chirp pulse with $A/2\pi = 100$ Hz and $\tau = 100$ ms, a hyperbolic tangent pulse with $A/2\pi = 100$ Hz, $\tau = 40$ ms, and $\eta = 1.5$, and a NOM pulse defined by $A/2\pi = 100$ Hz, $\nu = [1 \quad 2]$, $\gamma_0 = 10$, and $B/\gamma = 1\mathrm{e}-6$ T. The specific NOM, chirp, and hyperbolic tangent sweeps illustrated in Figure 1b and 1c are selected to demonstrate that each type of frequency sweep is capable of producing very similar M_x and M_y components over the same range of B_1 amplitudes (observed by noting that the M_x and M_y profiles track one another closely over the full range of B_1 in Figure 1b and 1c). Because each type of frequency sweep (NOM, chirp, hyperbolic tangent) can produce similar M_x and M_y profiles, it is advisable to favor the sweep that minimizes the pulse duration (factor 2) and power requirements (factor 3). Therefore, to compare the suitability of each sweep type for application in surface NMR, a synthetic comparison is conducted in which the duration and power requirements for a set of chirp and hyperbolic tangent pulses are compared against NOM pulses that produce similar M_x profiles. That is, for each chirp and hyperbolic tangent pulse, a NOM pulse producing a similar M_x profile is identified and the corresponding pulse durations and power requirements are compared. The power requirement is approximated as the integral of the square envelope of the current modulation $(\omega_1(t)/B)$ throughout the pulse; equivalent to treating the pulse power as $\sim I(t)^2$ for a peak current of 1 A.

Consider first a comparison between chirp and NOM pulses. A suite of chirp pulses described by all combinations of $A/2\pi = 50$, 100, 200, 400 Hz, $\tau = 30$–100 ms in steps of 5 ms, and $Q = 5, 10$ is formed and the corresponding M_x and M_y profiles are calculated. To identify a NOM pulse producing a similar net excitation over the same range of B_1 heterogeneity, two suites of NOM pulses are defined for $B/\gamma = 2\mathrm{e}-7$ T to $100\mathrm{e}-7$ T in steps of $1\mathrm{e}-7$ T, $\nu = 1$ to $\nu = \nu_{\max}$ for $\nu_{\max} = 1, 2$ and the same A, and the same Q, as the corresponding chirp pulse. That is, only chirp and NOM pulses that use the same A and Q are compared. The comparison is conducted once for a NOM pulse with $\gamma_0 = 4$ (black triangles and counts in Figure 3) and again for a NOM pulse with $\gamma_0 = 10$ (gray triangles and counts in Figure 3) to investigate the trend at two minimum adiabaticity levels. To conduct each comparison, a chirp pulse is selected and the NOM pulse producing a similar M_x profile is identified by comparing the chirp M_x profile against the M_x profiles produced by every NOM pulse. The pulse that minimizes the difference between the M_x profiles at B_1 strengths less than 10^{-5} is selected, and its pulse duration and power requirements are compared against that of the chirp pulse (to form a single triangle in Figure 3a and 3b and a single count in the histograms of Figure 3c–3f). Only the difference between the M_x profiles is minimized. We limit the comparison to the M_x profiles given that the primary motivation for the use of adiabatic pulses in this study is to exploit the coherent (single signed) M_x component to eliminate signal loss due to destructive interference. This also has the benefit of reducing complications related to the oscillatory behavior present in the M_y profile that

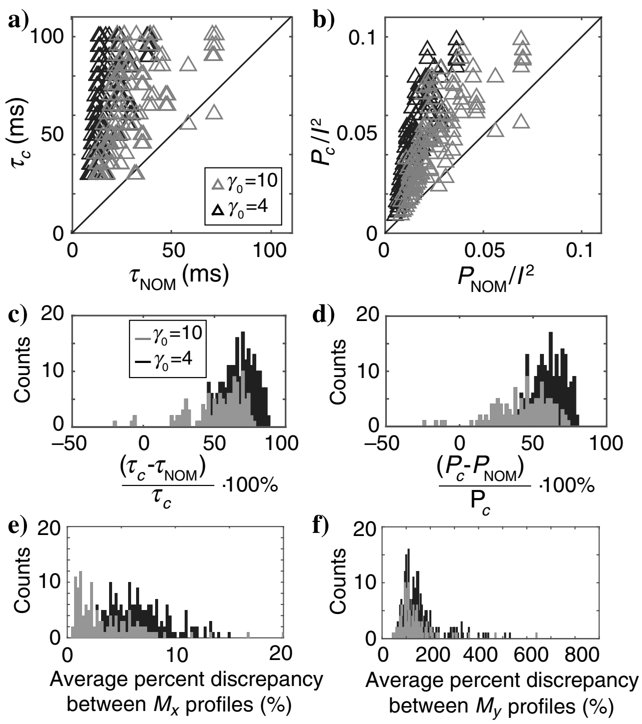

Figure 3. A comparison of the pulse duration and power requirements of NOM pulses and chirp pulses resulting in similar net excitation (i.e., similar M_x profiles at $B_1 < 1\mathrm{e}-5$ T). Each triangle in (a or b) or count in (c, d, e, or f) represents a comparison between a particular chirp pulse and a NOM pulse. The comparison is conducted once for a NOM pulse with a minimum adiabaticity of 4 (the black triangles and counts) and again with a minimum adiabaticity of 10 (the gray triangles and counts). (a and b) Comparison of the pulse duration and power requirements. (c and d) Percent reduction of the pulse duration or power requirement provided by the NOM pulse compared with the chirp pulse producing similar profiles. (e and f) Average percent discrepancy between the M_x and M_y profiles for each NOM pulse chirp pulse pair, respectively; the histograms indicate how similar the NOM and chirp M_x and M_y profiles are in each case.

depends strongly on the discretization of the B_1-axis. Only B_1 strengths less than 10^{-5} are considered in the comparison as this represents the B_1 present in most of the subsurface. In total, Figure 3 contains 240 comparisons between chirp and NOM adiabatic pulses. Figure 3a and 3b demonstrates that the NOM pulse consistently shortens the pulse duration and lowers the power required to produce similar M_x profiles as a chirp pulse (noted by observing that the triangles consistently fall above the 1-to-1 line). Figure 3c and 3d illustrates the percent reduction of the pulse duration and power requirement provided by the NOM pulse versus the chirp pulse. For the lower minimum adiabaticity case, consistent reductions of approximately 50%–90% are observed for the pulse duration and approximately 50%–80% are observed for the power consumption. For $\gamma_0 = 10$, the pulse duration and power reductions are smaller ranging from approximately 10% to 80% and 10%–70%, respectively. In some instances (for $\gamma_0 = 10$), the chirp pulse requires less power or a shorter duration (counts less than zero in Figure 3c and 3d), but this comes at the expense of lowering the minimum adiabaticity during the sweep. The M_x profiles in these cases are poor and do not reach one at the target B_1 amplitude. Figure 3e illustrates the average percent error between the chirp and NOM M_x profiles for each comparison; i.e., the x-coordinate shows the mean of the $|M_{x,\mathrm{NOM}} - M_{x,\mathrm{c}}|/|M_{x,\mathrm{c}}| \times 100\%$ vector. Most comparisons have less than a 10% discrepancy between the two M_x profiles. The $\gamma_0 = 10$ case better reproduces the chirp pulse results (smaller errors) than does the $\gamma_0 = 4$ case. Note that the discrepancy could be reduced by expanding the suite of NOM pulses used for the search. However, it is not expected to have a dramatic influence on the observed trends in Figure 3a–3d given that reducing the B/γ discretization further (when forming the suite of NOM pulses) was not observed to significantly vary the pulse durations and power requirements. Figure 3f illustrates the average percent discrepancy between the chirp and NOM M_y profiles for each comparison (i.e., the mean of the $|M_{y,\mathrm{NOM}} - M_{y,\mathrm{c}}|/|M_{y,\mathrm{c}}| \times 100\%$ vector). The differences in this case are much larger due to the strong oscillations present at large B_1 (e.g., Figure 1c) and because the main peak in the M_y profiles can be quite different. The comparison focuses on the M_x component; large M_y percent discrepancies do not indicate improved performance for the NOM or chirp pulses but simply that they produce different M_y profiles. Overall, NOM pulses are capable of producing similar M_x profiles as a chirp pulse, but they can do so using shorter pulses and less power.

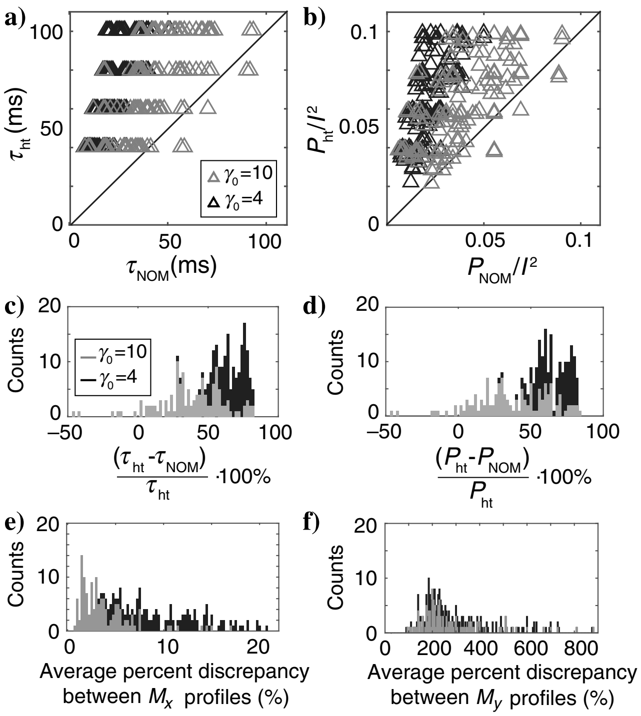

Figure 4. A comparison of the pulse duration and power requirements of NOM pulses and hyperbolic tangent pulses resulting in similar net excitation (i.e., similar M_x profiles at $B_1 < 1\mathrm{e}-5\ T$). Each triangle in (a or b) or count in (c, d, e, or f) represents a comparison between a particular hyperbolic tangent pulse and a NOM pulse. The comparison is conducted once for a NOM pulse with a minimum adiabaticity of 4 (black triangles and counts) and again with a minimum adiabaticity of 10 (gray triangles and counts). (a and b) Comparison of the pulse duration and power requirements. (c and d) Percent reduction of the pulse duration or power requirement provided by the NOM pulse compared with the hyperbolic tangent pulse producing similar profiles. (e and f) Average percent discrepancy between the M_x and M_y profiles for each NOM pulse hyperbolic tangent pulse pair, respectively; the histograms indicate how similar the NOM and hyperbolic tangent M_x and M_y profiles are in each case.

Figure 4 illustrates a similar comparison as Figure 3, in which NOM and hyperbolic tangent sweeps are now compared. A suite of hyperbolic tangent pulses described by all combinations of $A/2\pi = 50$, 100, 200, 400 Hz, $\tau = 40$–100 ms in steps of 20 ms, $\eta = 2 - 8$ in steps of 2, and $Q = 5$, 10 is formed and the corresponding M_x and M_y profiles calculated. A NOM pulse producing a similar M_x profile at $B_1 < 10^{-5}\ T$ is then identified using the same suite of NOM pulses as in the chirp pulse comparison. The comparison is conducted once for a NOM pulse with $\gamma_0 = 4$ (black triangles and counts in Figure 4) and again for a NOM pulse with $\gamma_0 = 10$ (gray triangles and counts in Figure 4). In total, Figure 4 contains 256 comparisons. Similar trends are observed as before; the NOM pulse consistently lowers the pulse duration and power required while producing a similar M_x profile as the hyperbolic tangent sweep (observed by noting that the triangles in Figure 4a and 4b consistently fall above the 1-to-1 line). For the lower minimum adiabaticity case, consistent reductions of approximately 50%–75% are observed for the pulse duration and the power consumption (Figure 4c and 4d). For $\gamma_0 = 10$, the pulse duration and power reductions are smaller ranging from approximately 0% to 60% (Figure 4c and 4d). For the higher adiabaticity case ($\gamma_0 = 10$), the hyperbolic tangent sweep is shorter than the corresponding NOM pulse in several instances. Figure 4e shows the percent discrepancy between the M_x profiles, where the $\gamma_0 = 10$ case reproduces the hyperbolic tangent profiles more closely than the $\gamma_0 = 4$ case. Figure 4f illustrates the average percent discrepancy between the hyperbolic tangent and NOM M_y profiles for each comparison; the M_y differences in this case are again much larger due to strong oscillation in the large B_1 limit and the differences in the main bump in the M_y profiles. Note that in some cases, the hyperbolic tangent sweep (primarily for large η and longer pulse durations) produces a large bump in the M_y profile at small B_1 (not shown). The current comparison does not reward this feature given that our focus is to exploit of the M_x component while minimizing the pulse duration. The growth of the M_y bump for the hyperbolic tangent case comes at the expense of an increased pulse duration, which in this study we chose to penalize. Further discussion regarding this M_y bump is given in the "Discussion" section. Overall, the NOM pulse is able to produce similar M_x profiles as the hyperbolic tangent sweep, but while shortening the pulse duration and reducing the required power.

Figures 3 and 4 indicate that the NOM approach is expected to reduce the pulse duration and power requirements necessary to produce similar M_x profiles compared with the chirp and hyperbolic tangent sweeps. However, we must still consider the utility of each pulse type for producing images of aquifer properties (factor 4). To contrast the ability of each adiabatic pulse to produce high-resolution images, Figures 5 and 6 illustrate the expected resolution as a function of depth in each case. The resolution is estimated using singular-value decomposition (SVD) of the surface NMR kernel matrix $\mathbf{K}$ (Müller-Petke and Yaramanci, 2008), where $\mathbf{K} = \mathbf{USV}^{\mathrm{T}}$. From the SVD, the resolution matrix $\mathbf{R}$ may be calculated ($\mathbf{R} = \mathbf{VV}^{\mathbf{T}}$). To evaluate the resolution as a function of depth, the full-width at half-maximum (FWHM) of each row in $\mathbf{R}$ is calculated (Müller-Petke and Yaramanci, 2008). The FWHM of each row in $\mathbf{R}$ provides a convenient metric to contrast the expected resolution for several adiabatic pulses simultaneously. To account for the noise when producing $\mathbf{R}$, only columns of $\mathbf{V}$ that correspond to singular values greater than the noise floor are included; i.e., a Picard plot is used to determine when the singular values should be truncated based upon the noise conditions (Fedi et al., 2005). In Figures 5 and 6, the data level is based upon 10 nV of random noise and a half-space of 30% water content. Note that when calculating the kernel, in each case the M_x and M_y components produced by the adiabatic pulses are included.

Consider first Figure 5, which illustrates the expected resolution provided by several adiabatic pulses for an amplitude-only inversion (i.e., the kernel considers only the amplitudes of the signal). The kernels correspond to a synthetic survey using a 75 m circular loop (coincident transmit/receive), 24 current amplitudes logarithmically spaced from 2 to 500 A, and a resistive subsurface. Kernels are generated using MRSMatlab (Müller-Petke et al., 2016). In each case, the kernel is formed using a different adiabatic pulse. The left, center, and right columns of Figure 5 each contrast five adiabatic pulses of equal duration (the left, center, and right columns correspond to durations of 38.8, 52.2, and 79.8 ms, respectively). Table 1 lists the parameters of all adiabatic pulses considered in Figure 5. In each column, two chirp pulses (red profiles) and two hyperbolic tangent pulses (green profiles) are compared against a NOM pulse (black profile). The top, middle, and bottom rows of Figure 5 illustrate the expected resolution as a function of depth, the magnitude of the singular values (i.e., the diagonal elements of $\mathbf{S}$), and the initial amplitudes produced by each pulse given a half-space of 30% water content, respectively. Comparing the resolution (Figure 5a–5c) for each pulse duration indicates that the NOM pulse consistently produces the sharpest resolution (given this noise level). This is noted by observing that the black profile is consistently closer to the y-axis (smaller x-values) than the red and green profiles. The solid green profile (the hyperbolic tangent pulse with $\eta = 4$) also consistently produces similar resolution as the NOM pulse. To gain insight into the expected resolution at alternate noise levels the rate of decay of the singular values can be considered (middle row of Figure 5). For each pulse duration, the singular values corresponding to the hyperbolic tangent pulse with $\eta = 4$ (the solid green profile) decay the slowest. This indicates that at higher noise levels, this pulse may include additional singular values when calculating $\mathbf{R}$ potentially improving resolution compared with the other pulses. At lower noise levels than that considered in Figure 5, similar results as Figure 5a–5c are produced. The bottom row contrasts the signal amplitudes produced in each case. The NOM and hyperbolic tangent pulse (with $\eta = 4$) consistently produce the largest signal amplitudes (while also providing the best resolution).

Figure 5 shows an amplitude-only inversion (the standard inversion scheme in surface NMR). However, Braun and Yaramanci (2005) demonstrate that considering the signal phase (i.e., a complex data) can improve resolution. To examine the performance of the same adiabatic pulses in the context of a complex inversion, Figure 6 illustrates the same resolution comparison as in Figure 5

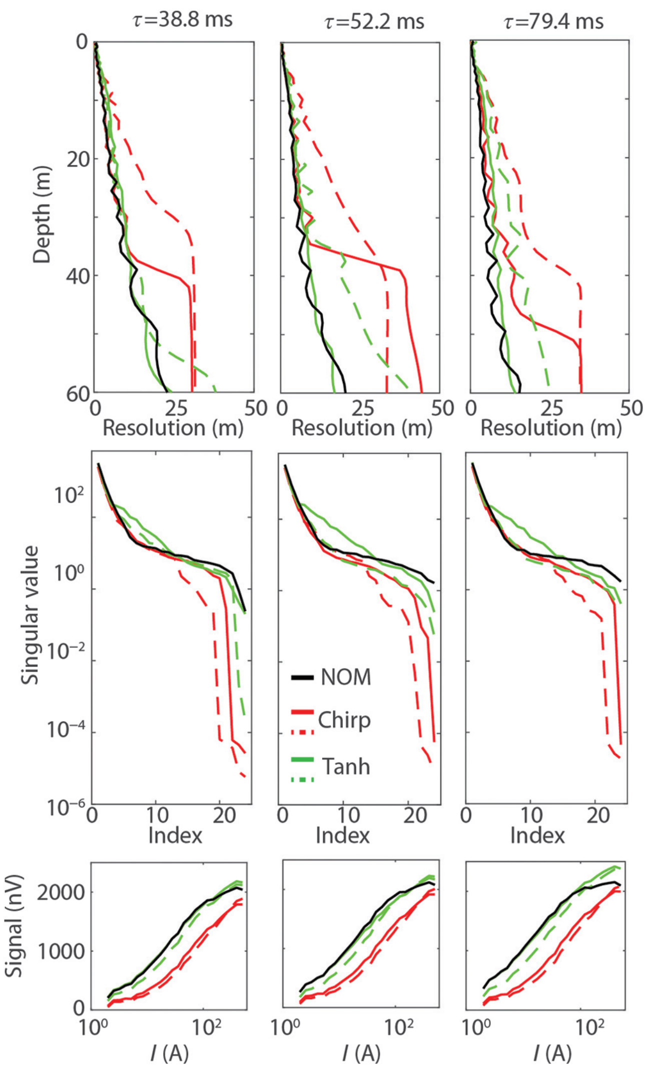

Figure 5. Resolution comparison among several NOM, hyperbolic tangent, and chirp pulses of equal pulse duration for the standard amplitude-only inversion (i.e., the kernel treats only the amplitudes). The adiabatic pulses in each column have the same pulse duration (listed at the top of the column). The top row illustrates the expected resolution as a function of depth for each AHP. The middle row illustrates the singular values of the kernel matrix for each AHP. The bottom row illustrates the sounding curves produced by each AHP for a resistive half-space of 30% water content. The parameters defining each AHP and the associated colors are listed in Table 1. NOM, hyperbolic tangent, and chirp pulses correspond to black, green, and red profiles, respectively.

but where the kernel now treats the real and imaginary components of the signal separately (instead of only considering the signal amplitudes). Table 1 lists the parameters defining the adiabatic pulses considered in each column of Figure 6. The top row of Figure 6 is similar to the top row of Figure 5, in which the NOM pulse (the black profiles) consistently provides the best resolution. Considering the singular values in each case (the middle row of Figure 6), the NOM pulse's singular values now appear to decay most slowly (except for the largest singular values, where the solid green profile initially decays more slowly). This suggests that the NOM pulse is likely to provide improved resolution for a wider range of noise levels for a complex inversion compared with the amplitude-only inversion. In the bottom row of Figure 6, the real and imaginary initial amplitudes are illustrated (for a 30% water content half-space); the imaginary components are positive, whereas the real components are given a negative sign for easier visualization (in practice, the sign can be manipulated by altering the frequency sweep). The NOM pulse consistently produces the largest imaginary signal (the component of the signal associated with M_x), whereas the hyperbolic tangent pulse produces the largest real signal (the component of the signal associated with M_y). Note that in Figures 5 and 6, the chirp pulses consistently produce the smallest signal amplitudes (for this case considering a half-space of 30% water content). Overall, Figures 5 and 6 indicate that the NOM pulse consistently provides better resolution and larger signal amplitudes than chirp and hyperbolic tangent pulses of equal duration. However, the hyperbolic tangent pulse with $\eta = 4$ produces similar levels of resolution as the NOM pulses for the amplitude-only inversion, and it is likely to provide better resolution than the NOM pulse in high noise environments.

Considering all four factors together, the NOM pulse is capable of producing similar M_x profiles as the chirp and hyperbolic tangent pulses but while doing so with shorter pulse durations and reduced power requirements (factors 1–3). The NOM pulse is also able to provide the best spatial resolution (factor 4) and largest signal amplitudes. Therefore, of the three investigated AHP pulse types (chirp, hyperbolic tangent, and NOM), we consider the NOM pulse to be best suited to surface NMR transmit conditions. To select a particular NOM pulse well-suited to surface NMR conditions, a sensitivity analysis of each parameter defining the NOM pulse is conducted in Appendix B. The NOM pulse investigated in the center columns of Figures 5 and 6 (defined by $B/\gamma = 3\mathrm{e}-7\ T$, $\gamma_0 = 4$, $A = 100$ Hz, and $\nu = 1$) is observed to provide a good balance among large signal amplitudes, high resolution, and a (reasonably) short pulse duration.

Field verification of a NOM pulse in surface NMR

To verify the feasibility of a NOM pulse under field conditions, a field study was conducted in Leque Island, Washington. The survey used a two turn 42 m circular coincident transmit and receive loop and 36 current amplitudes logarithmically sampled from approximately 1.75 to 296 A. The survey used a reference loop for noise cancellation and was conducted using the Vista Clara GMR system. The Larmor frequency at the site was observed to be 2290 Hz. The NOM pulse swept from 100 Hz below resonance ending at the Larmor frequency using the same frequency modulation function shown by the black line in Figure 2a (i.e., the NOM pulse investigated in the center columns of Figures 5 and 6). A 40 ms on-resonance data set was also collected to serve as a reference. Figure 7a illustrates the resulting sounding curves; the NOM and on-resonance sounding curves correspond to the black and gray lines, respectively. The NOM and on-resonance pulses produce similar amplitudes at low current amplitudes, whereas the NOM pulse improves the signal amplitude at strong currents.

Figure 7b and 7c shows the resulting water content and T_2* profiles, respectively. Inversion was performed using MRSMatlab (Müller-Petke et al., 2016). The standard QT amplitude-only inversion was used (Müller-Petke and Yaramanci, 2010). Both inversions were performed using the same level of regularization (value of 1000 in MRSMatlab) and were observed to fit the data to a similar level (Figure 7d and 7e). To form these profiles it was necessary to include RDP effects directly into the forward model, using the method proposed by Grombacher et al. (2017). Briefly, this process involves estimating the water content by matching the signal amplitude estimated at the end of the pulse with a kernel whose transverse magnetization term is determined by solving the Bloch equation with appropriately weighted relaxation terms. The appropriate weight for the relaxation terms is estimated from observed T_2* values. At this site, the observed decays were well-described by a T_2* of approximately 35 ms. Combined with the knowledge that the site is known to have strong magnetic effects (based on logging measurements near the site indicating $T_2 = 250$ ms), the component of the kernel describing the transverse magnetization at each location in the subsurface was formed by solving the Bloch equation with T_2 and T_1 equal to 250 ms (at all depths), and a background magnetic field distribution whose width is selected to correspond to $T_2* = 35$ ms. The same background field distribution was used for the on-resonance and NOM inversions to ensure each inversion was conducted with the same subsurface conditions. The exact value of the T_2 and T_1 is not observed to have a large impact on the modeled transverse magnetizations in this case given that

Table 1. Parameters defining the AHP pulses illustrated in each column of Figures 5 and 6. All AHP in a single column have the same pulse duration. The line color column indicates the colors of corresponding AHP pulses in Figures 5 and 6.

Line color	Left column	Center column	Right column
Black (NOM)	$A/2\pi = 100$ Hz, $\gamma_0 = 4$, $\nu_{\max} = 1$, $B/\gamma = 4\mathrm{e}-7\ T$	$A/2\pi = 100$ Hz, $\gamma_0 = 4$, $\nu_{\max} = 1$, $B/\gamma = 3\mathrm{e}-7\ T$	$A/2\pi = 100$ Hz, $\gamma_0 = 4$, $\nu_{\max} = 1$, $B/\gamma = 2\mathrm{e}-7\ T$
Solid red (chirp)	$A/2\pi = 100$ Hz, $\tau = 38.8$ ms	$A/2\pi = 100$ Hz, $\tau = 52.2$ ms	$A/2\pi = 100$ Hz, $\tau = 79.4$ ms
Dashed red (chirp)	$A/2\pi = 200$ Hz, $\tau = 38.8$ ms	$A/2\pi = 200$ Hz, $\tau = 52.2$ ms	$A/2\pi = 200$ Hz, $\tau = 79.4$ ms
Solid green (tanh)	$A/2\pi = 100$ Hz, $\eta = 4$, $\tau = 38.8$ ms	$A/2\pi = 100$ Hz, $\eta = 4$, $\tau = 52.2$ ms	$A/2\pi = 100$ Hz, $\eta = 4$, $\tau = 79.4$ ms
Dashed green (tanh)	$A/2\pi = 100$ Hz, $\eta = 2$, $\tau = 38.8$ ms	$A/2\pi = 100$ Hz, $\eta = 2$, $\tau = 52.2$ ms	$A/2\pi = 100$ Hz, $\eta = 2$, $\tau = 79.4$ ms

they are much larger than T_2*; i.e., magnetic effects dominate the RDP effects in this case not T_2 or T_1 processes. This alternative approach to account for RDP effects was necessary because the standard approach, which involves estimating the initial amplitude of the signal by extrapolating the observed decays to the midpoint of the pulse and using a kernel that neglects RDP effects (Walbrecker et al., 2009), leads to biased results for an adiabatic pulse in fast T_2* conditions (Grombacher et al., 2017).

Profiles are shown to a depth of 30 m given the high conductivity at the site (ranging from approximately 1 to 10 Ωm at depths shallower than 20 m) and the small coil diameter (42 m). The profiles have poor resolution below approximately 30 m depth. The resulting water content profiles (Figure 7b) both predict low water at the shallowest depths (consistent with a priori knowledge of the presence of a shallow clay layer) with an increasing water content beginning at approximately 4–5 m. Both profiles predict a peak in water content of approximately 30% at approximately 7–8 m in depth, with a drop in water content below this layer. At 15–20 m depth, the NOM profile predicts a lower water content than the on-resonance profile. At greater depths, the water content profiles converge predicting approximately 10%–15% water content. The T_2* profiles in both cases are very similar, showing little structure and values close to 30–35 ms at all depths. The predicted T_2* profiles are consistent with the RDP modeling assumption that assumed $T_2* = 35$ ms at all depths. Note that the RDP modeling does not constrain T_2* to be approximately 35 ms; it only affects the transverse magnetization term of the forward model. Despite some minor differences the on-resonance and NOM pulse produce similar results, whereas the NOM pulse provides a large signal enhancement for most pulse current amplitudes demonstrating the feasibility of the NOM pulse for current surface NMR hardware.

DISCUSSION

Adiabatic pulses provide an excitation scheme capable of enhancing the signal amplitude in surface NMR. To ensure that the advantages of the AHP pulse can be fully exploited in surface NMR, adiabatic pulses that perform well in surface NMR transmit conditions must be selected. Synthetic comparison between the two types of AHP previously implemented in surface NMR (chirp and hyperbolic tangent pulses) and an alternative adiabatic pulse defined using the NOM approach indicates that the NOM pulse is better suited to surface NMR transmit conditions when considering the scenario in which ω_1 is coupled to the instantaneous $\Delta\omega$. Recommendation of the NOM approach for adiabatic pulses in surface NMR is based upon a desire to exploit the coherent M_x component produced by an AHP pulse while limiting the pulse duration. The NOM approach is well-suited to this goal given that it implicitly balances a desire to produce the fastest possible sweep with the need to ensure a minimum level of adiabaticity is maintained. Figures 3–6 demonstrate that the NOM approach is capable of producing similar M_x profiles as the chirp and hyperbolic tangent pulses using shorter pulse durations and less power, while also providing large signal amplitudes and sharp resolution. However, if an amplitude-only inversion is to be used in high noise conditions, the hyperbolic tangent pulse with $\eta = 4$ may be preferable to the investigated NOM pulses. Comparison of the chirp and hyperbolic tangent pulses in Figures 5 and 6 indicates that the hyperbolic tangent pulse is expected to improve the signal amplitudes and resolution compared with the chirp pulse. Therefore, if the proposed NOM approach is not available, we recommend that the hyperbolic tangent pulse (with $\eta = 4$) be selected in place of the chirp pulse.

Another advantage of the NOM approach is the manner in which the pulse is parameterized. Conceptually, it is straightforward to understand the meaning of the B, ν, and γ_0 parameters and how they are expected to impact the performance of the NOM pulse. They specify the range of B_1 over which a specific adiabaticity requirement must be guaranteed. In contrast, for the chirp and hyperbolic tangent sweeps, it is less straightforward to immediately

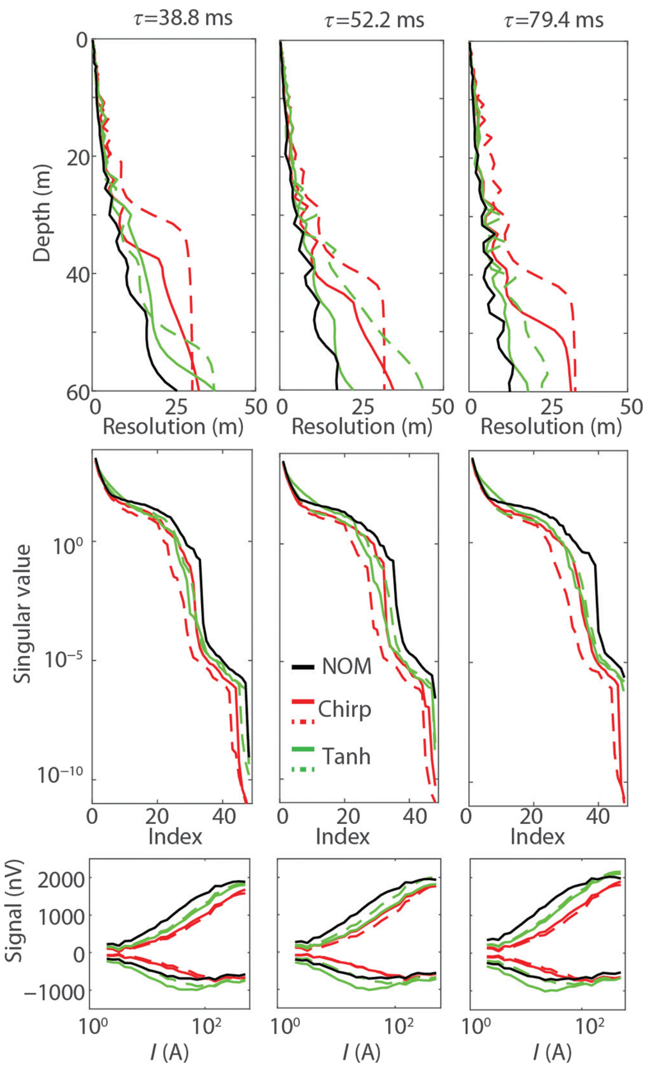

Figure 6. Resolution comparison among several NOM, hyperbolic tangent, and chirp pulses of equal pulse duration for the complex inversion (i.e., the kernel treats the real and imaginary components separately). The adiabatic pulses in each column have the same pulse duration (listed at the top of the column). The top row illustrates the expected resolution as a function of depth for each AHP. The middle row illustrates the singular values of the kernel matrix for each AHP. The bottom row illustrates the sounding curves produced by each AHP for a resistive half-space of 30% water content (imaginary components have a positive sign, whereas the real components have a negative sign for easier visualization). The parameters defining each AHP and the associated colors are listed in Table 1 (the same AHP as in Figure 5 are investigated). NOM, hyperbolic tangent, and chirp pulses correspond to the black, green, and red profiles, respectively.

understand the impact that τ and η will have on the final performance of the pulse; that is, it is not straightforward to translate τ and η into estimates of the range of B_1 over which the pulse will perform well and the expected adiabaticity throughout the sweep.

Note that the comparisons among the NOM, chirp, and hyperbolic sweeps in Figures 3 and 4 were based on M_x components; the M_y differences were not considered. In practice, the M_y component also contributes to the signal amplitude and resolution, but given that our goal was to exploit the coherent M_x component, the M_y component is considered secondary for the pulse duration and power requirement comparison. However, the M_x and M_y components are included in the resolution comparison as shown in Figures 5 and 6. For the hyperbolic tangent sweep, the M_y component in some cases contains a large bump at low B_1 (even lower B_1 than the location of the main M_x bump). The source of this bump can be understood by considering the hyperbolic tangent sweep to be effectively composed of two pulses. The first describes the initial frequency sweep ending when $\Delta\omega$ is close to zero and is effectively responsible for producing the M_x profile. For long duration pulses with large η, this part ends relatively early in the pulse. The second part can be considered as an on-resonance pulse (because $\Delta\omega$ is so small during the very slow approach to resonance) performed using the residual magnetization left in the B_0 direction. During the second part, the transverse magnetization produced by the first part is effectively spin locked to the B_1 axis and is largely unaffected by the long tail of the hyperbolic tangent sweep. The large M_y bump is useful for improving signal amplitudes and resolution (as evidenced by the similar signal amplitudes and resolution shown by the NOM and hyperbolic tangent pulse with $\eta = 4$ in Figure 5). However, the growth of the M_y bump comes at the expense of an increased pulse duration. Furthermore, the M_x component is likely very sensitive to RDP effects in this case given that it spends most of the pulse duration lying fully in the transverse plane locked to the B_1 axis exposed to T_2 processes. We prefer to prioritize short pulse durations over a large M_y bump given that the latter may increase power requirements and potentially enhance RDP.

When deciding if an adiabatic pulse should be used in place of an on-resonance pulse (or other transmit approaches such as frequency cycling) several factors should be considered. First, adiabatic pulses are likely to require longer pulse durations than an on-resonance pulse to achieve similar depth penetrations. This may lead to enhanced RDP compared with an on-resonance pulse (primarily in the fast T_2 limit). In these cases, signal attenuation due to RDP may cancel out the signal enhancements provided by the adiabatic pulse. That is, the shorter on-resonance pulse may produce larger signal amplitudes because RDP may affect the adiabatic pulse more severely. If short T_2 are suspected, the NOM pulse should be designed using smaller B to reduce the pulse duration. The shorter pulse duration will come at the expense of reducing the depth penetration and signal amplitude.

Another trade-off when using adiabatic pulses instead of on-resonance pulses is that the increased signal amplitude requires heightened power consumption. The on-resonance approach represents the most efficient means of generating a transverse magnetization. On-resonance pulses will be able to generate a fully transverse magnetization at smaller B_1 amplitudes given a fixed amount of available power. Adiabatic pulses offer larger signal amplitudes but require larger maximum power to ensure adequate depth penetration. One approach to maximize depth penetration given a fixed peak power may be to pair several on-resonance pulses (with large current amplitudes) with the adiabatic soundings to improve sensitivity at the greatest depths. The increased power consumption of the adiabatic pulse may also require more charge cycles for the capacitors used to source the bus voltage during transmit, which may increase survey times. However, this increase in survey time is likely compensated by the adiabatic pulse's S/N improvement reducing the number of stacks necessary.

In environments in which the Larmor frequency is uncertain and/or strong background magnetic field inhomogeneity is present (e.g., magnetic environments) one should consider whether the S/N improvement of the adiabatic pulse is trumped by the heightened modeling accuracy provided by the frequency-cycling technique (Grombacher et al., 2016). Frequency-cycling (which uses off-resonance pulses) can help alleviate sensitivity to a poor Larmor frequency estimate and minimize

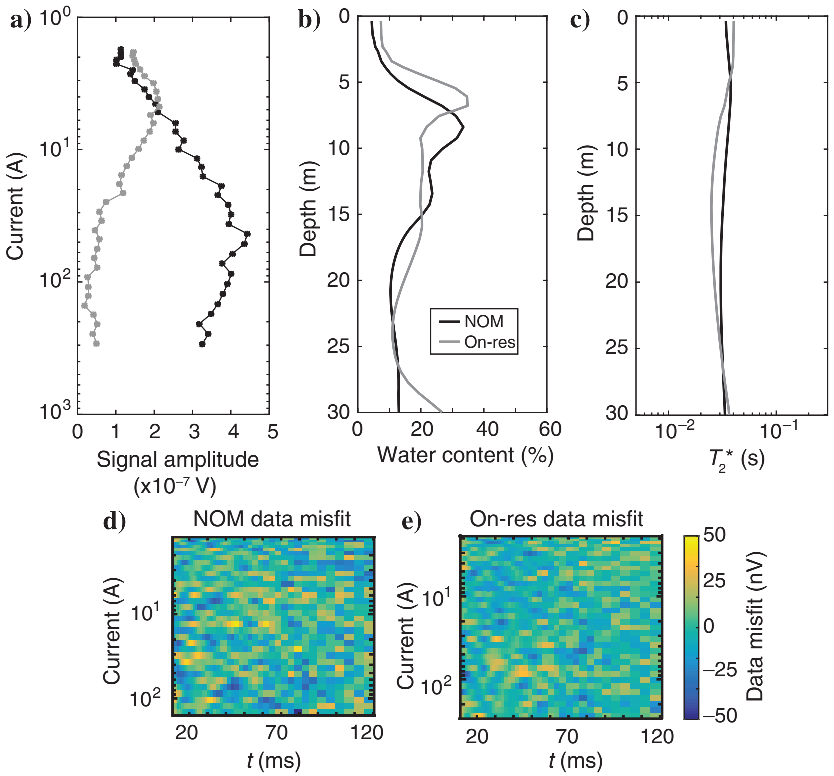

Figure 7. Results of a field survey using the recommended NOM adiabatic pulse ($A/2\pi = 100$ Hz, $\gamma_0 = 4$, $v = 1$, $B/\gamma = 3\mathrm{e}-7\ T$) conducted at Leque Island, Washington. The results of a survey using a 40 ms on-resonance pulse are also shown as a reference. (a) Sounding curves for the NOM (black) and 40 ms on-resonance pulse (gray). (b) Water content profiles produced by the NOM (black) and on-resonance (gray) pulses. (c) T_2* profiles produced by the NOM (black) and on-resonance (gray) surveys. (d and e) Data misfit for the NOM and on-resonance inversions that correspond to the profiles shown in (b and c), respectively.

potential artifacts in the estimated water content profile that arise from unknown off-resonance effects. Grunewald et al. (2016) suggest an approach similar to frequency cycling that may be used with adiabatic pulses, in which a pair of adiabatic pulses is formed by first sweeping from below resonance and then again from above resonance. This allows the sign of the M_x component to be alternated, whereas the sign of the M_y component remains fixed. This potentially allows the data to be stacked in a manner that reduces the impact of an uncertain Larmor frequency. Investigation of the utility of this approach to alleviate sensitivity to an uncertain Larmor frequency will be the subject of future research.

To summarize, the decision to use an adiabatic pulse should involve consideration of RDP, depth penetration, and Larmor frequency uncertainty. The excitation scheme selected for a particular field study should choose a strategy optimally suited for local conditions. Also important to note is that the benefits of using an adiabatic pulse can be exploited in parallel with all existing noise cancellation approaches.

We consider only AHP pulses in this work as our focus is the excitation portion of a surface NMR FID measurement. Alternative adiabatic pulses that function as inversion pulses (Baum et al., 1985; Grunewald and Walsh, 2013b), or phase preserving plane rotations (i.e., refocusing pulses; Conolly et al., 1989) may also have applications for other surface NMR pulse sequences. The application of these alternative adiabatic pulses in surface NMR will be the focus of future research.

CONCLUSION

Adiabatic pulses are capable of enhancing the S/N in surface NMR. To ensure efficient implementation of adiabatic pulses into the surface NMR framework, a NOM approach is used to design pulses specifically intended for surface NMR conditions. This approach implicitly balances a desire to build a pulse that produces a large signal amplitude given a heterogeneous applied magnetic field with the need to ensure a minimum level of adiabaticity is maintained throughout; producing the shortest duration pulse that ensures a minimum adiabaticity is maintained over a specified B_1 range. The performance of the NOM pulse is compared against alternative adiabatic pulses described by linear (chirp) and hyperbolic tangent sweeps, and it is observed to provide an equivalent ability to generate a transverse magnetization (M_x component) while reducing the pulse duration and power requirements. The NOM approach is also observed to provide sharp resolution and large signal amplitudes. An additional advantage of the NOM approach is that it presents an intuitive parameterization, allowing straightforward control of the range of B_1 in which the pulse performs optimally. Comparing the two previously used adiabatic pulses (chirp and hyperbolic tangent) demonstrates that the hyperbolic tangent pulse provides better resolution and larger signal amplitudes compared with the chirp pulse. Note that the hyperbolic tangent pulse defined by $\eta = 4$ produces similar levels of resolution and signal amplitudes as the investigated NOM pulses for an amplitude-only inversion.

The NOM pulse defined by $A/2\pi = 100$ Hz, $B/\gamma = 3\mathrm{e}-7$ T, $\gamma_0 = 4$, and $\nu = 1$ was observed to provide a good balance between improved signal amplitude, high resolution, and relatively short pulse duration. For integration into the surface NMR experimental protocol, we recommend the implementation of a single NOM pulse, in which the depth sensitivity is controlled by varying the peak current amplitude similar to the traditional on-resonance sounding approach. Ultimately, the NOM approach presents an opportunity to improve S/N in surface NMR, expanding the range of conditions in which the technique may be used.

ACKNOWLEDGMENTS

D. Grombacher was supported by funding from a Danish Council for Independent Research Postdoctoral Grant (DFF-5051-00002). The author would like to thank E. Grunewald for the collection of the surface NMR field data. MRSMatlab was used to forward model/invert all synthetic and field surface NMR data (Müller-Petke et al., 2016).

APPENDIX A

DETERMINING THE FREQUENCY SWEEP USING THE NOM APPROACH FOR SURFACE NMR TRANSMIT CONDITIONS

The NOM approach provides the ability to determine the fastest possible frequency sweep satisfying a minimum acceptable adiabaticity level over a particular B_1 range given fixed shapes of the $\Delta\omega(t)$ and $\omega_1(t)$ functions. For the scenario in which the transmit coil's frequency response is used to modulate the current amplitude, the shape of the $\Delta\omega(t)$ and $\omega_1(t)$ functions can be described by a parametric function of time $\xi(t)$, where

$$\Delta\omega(t) = A\xi(t), \text{ and } \omega_1(t) = \frac{C}{\pi}\frac{T/2}{(A\xi(t))^2 + \left(\frac{T}{2}\right)^2}, \ \xi\varepsilon[1,0]. \tag{A-1}$$

This describes the situation in which the transmit frequency can be freely modulated, but its amplitude is coupled to the instantaneous transmit frequency via the coil response. The coil response in equation A-1 is modeled as a Lorentzian. The T term is the FWHM of the Lorentzian, and it is related to the coil quality factor Q. The C term is used to scale the magnitude of $\omega_1(t)$ when $\Delta\omega = 0$ ($\omega_1 = \gamma B_1$ when $\Delta\omega = 0$). The boundary conditions of $\xi(t)$ ($\xi(t=0) = 1$ and $\xi(t=\tau) = 0$) are selected to ensure that $\Delta\omega_{\mathrm{NOM}}(t)$ begins at an initial offset equal to A and sweeps toward zero at the end of the pulse (as required for an AHP). To determine $\xi(t)$ using the NOM approach, equation 2 is rewritten in the following form (accomplished by expanding equation 2 using equation 1) (Rosenfeld et al., 1997):

$$\Gamma(\omega_0, t) = \frac{(\nu^2\omega_1^2 + \Delta\omega^2)^{3/2}}{\nu|\Delta\omega\dot{\omega}_1 - \omega_1\dot{\Delta\omega}|}. \tag{A-2}$$

The ν factor is used to describe the B_1 range where Γ cannot drop below a specified minimum. Substitution of equation A-1 into A-2 gives

$$\Gamma(t) = \frac{\left(\frac{\nu^2 B^2 (T/2)^4}{((A\xi(t))^2 + (T/2)^2)^2} A^2\xi(t)^2\right)^{3/2}}{\nu\dot{\xi}\left|\frac{2AB(T/2)^2(A\xi(t))^2}{((A\xi(t))^2+(T/2)^2)^2} + \frac{AB(T/2)^2}{(A\xi(t))^2+(T/2)^2}\right|}, \tag{A-3}$$

where we have assumed that the time derivative of $\xi(t)$ (denoted by $\dot{\xi}$) is negative (i.e., $\xi(t)$ is monotonically decreasing from 1 to 0). To ensure a minimum adiabaticity γ_0, we require

$$\Gamma(t) \geq \gamma_0. \tag{A-4}$$

Combining equations A-3 and A-4 and rearranging for $\dot{\xi}$ yields

$$\frac{d\xi}{dt} \geq \frac{1}{\gamma_0} f(\xi, \nu), \tag{A-5}$$

where $f(\xi, \nu)$ is equal to all terms on the right side of equation A-3 excluding $\dot{\xi}$. To satisfy equation A-4, the minimum of $f(\xi, \nu)$ for all values of ν ($\nu_{\min}$ and $\nu_{\max}$ are used to specify a B_1 range where equation A-4 must be satisfied) is calculated. Given the minimum value of $f(\xi, \nu)$ for each ξ, the optimal timing is found by integrating equation A-5 to give

$$t(\xi) = \gamma_0 \int_1^{\xi} d\xi' \min(f(\xi', \nu))^{-1}. \tag{A-6}$$

Once the timing of the sweep is known, $\Delta\omega_{\mathrm{NOM}}(t)$ is known.

APPENDIX B

SELECTING A PARTICULAR NOM PULSE WELL-SUITED TO SURFACE NMR CONDITIONS

To select a suitable NOM pulse for surface NMR (for the scenario in which ω_1 is coupled to the instantaneous $\Delta\omega$) appropriate A, γ_0, ν, and B values must be determined. This requires balancing a desire to improve the signal amplitude while ensuring that the pulse duration does not become excessive. Figure B-1 illustrates a simple sensitivity analysis of the M_x profile to each parameter defining the NOM pulse; for each row, one of the parameters is varied and the others are held fixed. This approach provides a simple means to identify a narrow range of parameters expected to perform well. Table B-1 defines the parameters used in each row of Figure B-1. The top row illustrates the influence of the A parameter. Increasing A has little influence on the M_x profile at small B_1 but does improve performance at larger B_1. Larger A also results in longer pulse durations (Figure B-1b). Given that the B_1 range (large B_1) that displays sensitivity to A is only present in the subsurface for strong currents and/or close to the coil, we recommend selection of small A (e.g., $A/2\pi = 100$ Hz). This reduces the pulse duration without affecting performance at small B_1. Figure B-1c indicates that the selection of the minimum adiabaticity plays a strong role in controlling the effectiveness of the adiabatic pulse in a heterogeneous B_1. For low γ_0 (e.g., $\gamma_0 < \sim 3$, darkest profiles), the M_x profile

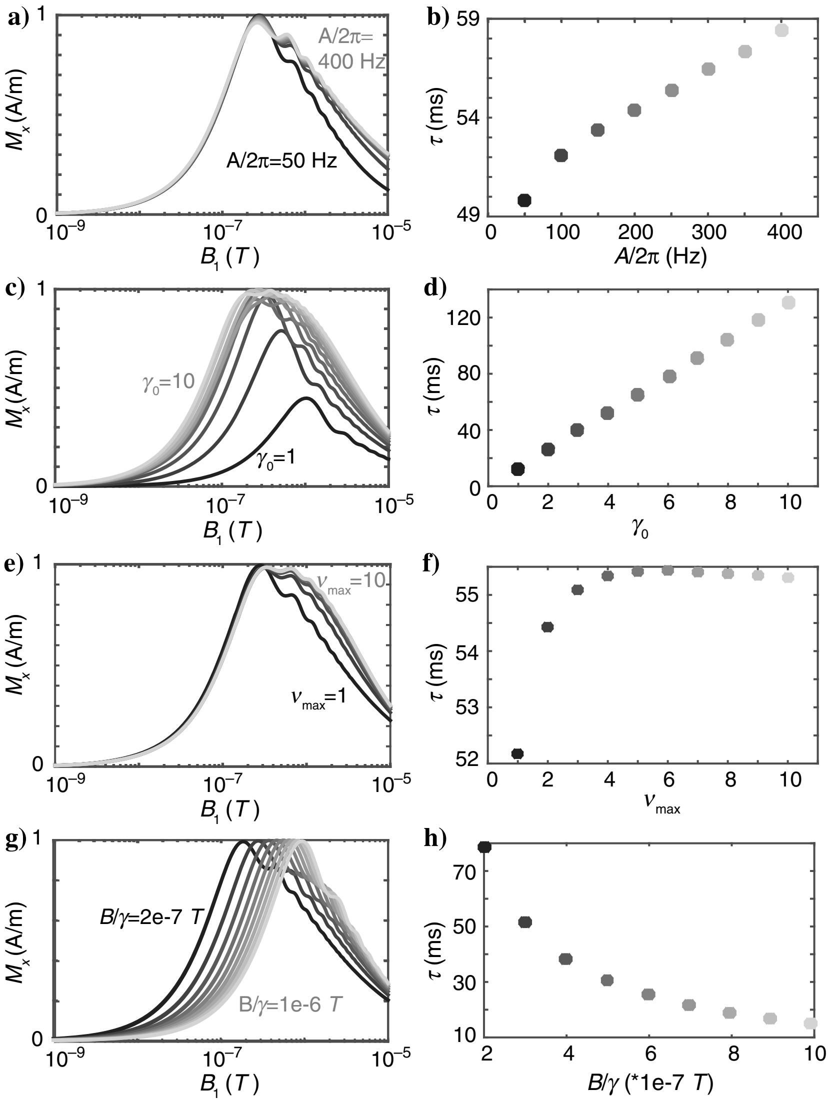

Figure B-1. A sensitivity analysis demonstrating the impact of each parameter defining the NOM pulse on the expected M_x profiles (left column) and the resulting duration of the NOM pulse (right column). The first, second, third, and fourth rows illustrate the sensitivity to the A, γ_0, ν, and B parameters, respectively. Only one parameter is varied within a single row; Table B-1 indicates the parameters used to form all NOM pulses in each row. The black and gray profiles or dots correspond to small and large values of each parameter; $Q = 10$ in all cases.

Table B-1. Parameters defining the NOM pulses illustrated in Figure B-1.

	Figure B-1a and B-1b	Figure B-1c and B-1d	Figure B-1e and B-1f	Figure B-1g and B-1h
$A/2\pi$	50:50:400	100	100	100
γ_0	4	1:10	4	4
$\nu_{\max}$ ($\nu = [1 \nu_{\max}]$)	1	1	1:1:10	1
$B/\gamma * 1\mathrm{e}-7$	3	3	3	2:1:10

is poor and does not reach one at the target B_1 amplitude of 3e − 7 T. As γ_0 increases, the M_x profile broadens and the pulse produces a fully transverse magnetization over a greater range of B_1. Figure B-1d shows that this improved performance results comes at the cost of an increased pulse duration, in which extremely long pulses result if large γ_0 is selected. We recommend selection of $\gamma_0 = 4$, given that it provides a balance between $M_x \sim 1$ at the target B_1 amplitude and a shorter pulse duration. Figure B-1e illustrates the sensitivity of the M_x profile to ν. In each case, the minimum adiabaticity is ensured over a B_1 range equal to 3e − 7 T to $\nu_{\max} *$ 3e − 7 T, where $\nu_{\max} = 1 - 10$. Increasing $\nu_{\max}$ is observed to extend the M_x profile to larger B_1, while requiring a modest increase in the pulse duration (Figure B-1f). Similar to the A parameter, the B_1 region displaying sensitivity to ν is primarily present at shallow depths and/or for large currents. Therefore, we recommend selecting $\nu = 1$; this simplifies the design of the pulse by allowing the selection of B to specify the target B_1. The final parameter that needs to be specified is B. Figure B-1g illustrates that B strongly influences the M_x profile's position. Selecting B specifies the B_1 amplitude at which the minimum adiabaticity is ensured, effectively allowing the range of B_1 in which the adiabatic pulse performs as desired to be controlled. Ensuring the minimum adiabaticity at smaller B_1 amplitudes (i.e., small B values) requires longer pulse durations (Figure B-1h). However, prior to selection of a B parameter, we must also ensure that the corresponding NOM pulse is capable of producing large signal amplitudes and high-resolution images for surface NMR conditions. Figures 5 and 6 provide insight into the performance for NOM pulses defined by several different B values (B/γ = 4e − 7 T [left columns], 3e − 7 T [center columns], and 2e − 7 T [right columns]). Decreasing B is observed to improve resolution and increase the signal amplitude (for this 30% water content half-space example). To balance a desire for sharp resolution and large signal amplitudes with a reasonable pulse duration, we recommend selecting B = 3e − 7 T. To summarize, we recommend the use of a NOM pulse defined by $A/2\pi = 100$ Hz, $\gamma_0 = 4$, $\nu = 1$, and B/γ = 3e − 7 T (the NOM pulse investigated in the center columns of Figures 5 and 6). The $\Delta\omega(t)$ function corresponding to this pulse is also shown by the black line in Figure 2a. Note that this set of parameters does not define the optimal NOM pulse for all conditions; it defines a NOM pulse expected to provide reliable performance while balancing several competing desires (e.g., large signal amplitudes versus short pulse duration).

REFERENCES

Baum, J., R. Tycko, and A. Pines, 1985, Broadband and adiabatic inversion of a two-level system by phase modulated pulses: Physical Review A, **32**, 3435–3447, doi: 10.1103/PhysRevA.32.3435.

Behroozmand, A. A., K. Keating, and E. Auken, 2015, A review of the principles and applications of the NMR technique for near-surface characterization: Surveys in Geophysics, **36**, 27–85, doi: 10.1007/s10712-014-9304-0.

Bendall, M. R., and D. T. Pegg, 1986, Uniform sample excitation with surface coils for in vivo spectroscopy by adiabatic rapid half passage: Journal of Magnetic Resonance, **67**, 376–381.

Bloch, F., 1946, Nuclear induction: Physical Review, **70**, 460–474, doi: 10.1103/PhysRev.70.460.

Braun, M., and U. Yaramanci, 2005, Study on complex inversion of magnetic resonance sounding signals: Near Surface Geophysics, **3**, 155–163, doi: 10.3997/1873-0604.2005011.

Conolly, S., D. Nishimura, and A. Macovski, 1989, A selective adiabatic spin-echo pulse: Journal of Magnetic Resonance, **83**, 324–334.

Costabel, S., and M. Müller-Petke, 2014, Despiking of magnetic resonance signals in time and wavelet domains: Near Surface Geophysics, **12**, 185–197, doi: 10.3997/1873-0604.2013027.

Dalgaard, E., E. Auken, and J. J. Larsen, 2012, Adaptive noise cancelling of multichannel magnetic resonance sounding signals: Geophysical Journal International, **191**, 88–100, doi: 10.1111/j.1365-246X.2012.05618.x.

Fedi, M., P. C. Hansen, and V. Poaletti, 2005, Analysis of depth resolution in potential-field inversion: Geophysics, **70**, no. 6, A1–A11, doi: 10.1190/1.2122408.

Garwood, M., and L. Delabarre, 2001, The return of the frequency sweep: Designing adiabatic pulses for contemporary NMR: Journal of Magnetic Resonance, **153**, 155–177, doi: 10.1006/jmre.2001.2340.

Garwood, M., and Y. Ke, 1991, Symmetric pulses to induce arbitrary flip angles with compensation for RF inhomogeneity and resonance offsets: Journal of Magnetic Resonance, **94**, 511–525.

Grombacher, D., A. A. Behroozmand, and E. Auken, 2017, Accounting for relaxation during pulse effects for long pulses and fast relaxation times in surface nuclear magnetic resonance: Geophysics, **82**, no. 6, JM23–JM36.

Grombacher, D., M. Müller-Petke, and R. Knight, 2016, Frequency cycling for compensation of undesired off-resonance effects in surface nuclear magnetic resonance: Geophysics, **81**, no. 4, WB33–WB48, doi: 10.1190/geo2015-0181.1.

Grombacher, D., J. O. Walbrecker, and R. Knight, 2014, Imparting a phase during excitation for improved resolution in surface nuclear magnetic resonance: Geophysics, **79**, no. 6, E329–E339, doi: 10.1190/geo2013-0452.1.

Grunewald, E., D. Grombacher, and D. O. Walsh, 2016, Adiabatic pulses enhance surface nuclear magnetic resonance measurements and survey speed for groundwater investigations: Geophysics, **81**, no. 4, WB85–WB96, doi: 10.1190/geo2015-0527.1.

Grunewald, E., R. Knight, and D. Walsh, 2014, Advancement and validation of surface nuclear magnetic resonance spin-echo measurements of T_2: Geophysics, **79**, no. 2, EN15–EN23, doi: 10.1190/geo2013-0105.1.

Grunewald, E., and D. O. Walsh, 2013a, Multiecho scheme advances surface NMR for aquifer characterization: Geophysical Review Letters, **40**, 6346–6350, doi: 10.1002/2013GL057607.

Grunewald, E., and D. O. Walsh, 2013b, Relaxation time estimation in surface NMR: U.S. Patent 13/750,984.

Halse, M. E., and P. T. Callaghan, 2008, A dynamic nuclear polarization strategy for multi-dimensional Earth's field NMR spectroscopy: Journal of Magnetic Resonance, **195**, 162–168, doi: 10.1016/j.jmr.2008.09.007.

Larsen, J. J., 2016, Model-based subtraction of spikes from surface nuclear magnetic resonance data: Geophysics, **81**, no. **4**, WB1–WB8, doi: 10.1190/geo2015-0442.1.

Larsen, J. J., E. Dalgaard, and E. Auken, 2014, Noise cancelling of MRS signals combining model-based removal of powerline harmonics and multichannel Wiener filtering: Geophysical Journal International, **196**, 828–836, doi: 10.1093/gji/ggt422.

Legchenko, A., 2007, MRS measurements and inversion in presence of EM noise: Boletin Geologico y Minero, **118**, 489–508.

Legchenko, A., J. M. Baltassat, A. Bobachev, C. Martin, H. Robain, and J. M. Vouillamoz, 2004, Magnetic resonance sounding applied to aquifer characterization: Ground Water, **42**, 363–373, doi: 10.1111/j.1745-6584.2004.tb02684.x.

Legchenko, A., and P. Valla, 2002, A review of the basic principles for proton magnetic resonance sounding measurements: Journal of Applied Geophysics, **50**, 3–19, doi: 10.1016/S0926-9851(02)00127-1.

Legchenko, A., J. M. Vouillamoz, and J. Roy, 2010, Applications of the magnetic resonance sounding method to the investigation of aquifers in the presence of magnetic materials: Geophysics, **75**, no. 6, L91–L100, doi: 10.1190/1.3494596.

Levitt, M., 2008, Spin dynamics basics of nuclear magnetic resonance: John Wiley &Sons Ltd.

Mohnke, O., and U. Yaramanci, 2008, Pore size distributions and hydraulic conductivities of rocks derived from magnetic resonance sounding relaxation data using multi-exponential decay time inversion: Journal of Applied Geophysics, **66**, 73–81, doi: 10.1016/j.jappgeo.2008.05.002.

Müller-Petke, M., M. Braun, M. Hertrich, S. Costabel, and J. Walbrecker, 2016, MRSmatlab — A software tool for processing, and inversion of magnetic resonance sounding data: Geophysics, **81**, no. 4, WB9–WB21, doi: 10.1190/geo2015-0461.1.

Müller-Petke, M., and S. Costabel, 2013, Surface-NMR in urban area — A no go?: Near Surface Geoscience 2013 Meeting, doi: 10.3997/2214-4609.20131367.

Müller-Petke, M., and S. Costabel, 2014, Comparison and optimal parameter settings of reference based harmonic noise cancellation in time and frequency domains for surface NMR: Near Surface Geophysics, **12**, 199–210.

Müller-Petke, M., and U. Yaramanci, 2008, Resolution studies for magnetic resonance sounding (MRS) using the singular value decomposition: Journal of Applied Geophysics, **66**, 165–175, doi: 10.1016/j.jappgeo.2007.11.004.

Müller-Petke, M., and U. Yaramanci, 2010, QT inversion — Comprehensive use of the complete surface NMR data set: Geophysics, **75**, no. 4, WA199–WA209, doi: 10.1190/1.3471523.

Rosenfeld, D., S. L. Panfil, and Y. Zur, 1997, Optimization of adiabatic selective pulses: Journal of Magnetic Resonance, **126**, 221–228, doi: 10.1006/jmre.1997.1165.

Shushakov, O. A., 1996, Surface NMR measurement of proton relaxation times in medium to coarse-grained sand aquifer: Magnetic Resonance Imaging, **14**, 959–960, doi: 10.1016/S0730-725X(96)00194-4.

Skinner, T. E., and P-M. L. Robitaille, 1992, General solutions for tailored modulation profiles in adiabatic excitation: Journal of Magnetic Resonance, **98**, 14–23.

Silver, M. S., R. I. Joseph, and D. I. Hoult, 1984, Highly selective $\pi/2$ and π pulse generation: Journal of Magnetic Resonance, **59**, 347–351.

Tannus, A., and M. Garwood, 1997, Adiabatic pulses: NMR in Biomedicine, **10**, 423–434, doi: 10.1002/(ISSN)1099-1492.

Town, G., and D. Rosenfeld, 1990, Analytic solutions to adiabatic pulse modulation functions optimized for inhomogeneous B_1 fields: Journal of Magnetic Resonance, **89**, 170–175.

Trushkin, D. V., O. A. Sushakov, and A. V. Legchenko, 1994, The potential for a noise-reducing antenna for surface NMR groundwater surveys in the earth's magnetic field: Geophysical Prospecting, **42**, 855–862, doi: 10.1111/j.1365-2478.1994.tb00245.x.

Ugurbil, K., M. Garwood, and M. R. Bendall, 1987, Amplitude- and frequency-modulated pulses to achieve 90° plane rotations with inhomogeneous B_1 fields: Journal of Magnetic Resonance, **82**, 177–185.

Ugurbil, K., M. Garwood, and A. R. Rath, 1988, Optimization of modulation functions to improve insensitivity of adiabatic pulses to variations in B_1 magnitude: Journal of Magnetic Resonance, **80**, 448–469.

Walbrecker, J. O., M. Hertrich, and A. G. Green, 2009, Accounting for relaxation processes during the pulse for surface NMR data: Geophysics, **74**, no. 6, G27–G34, doi: 10.1190/1.3238366.

Walbrecker, J. O., M. Hertrich, J. A. Lehmann-Horn, and A. G. Green, 2011, Estimating the longitudinal relaxation time T_1 in surface NMR: Geophysics, **76**, no. 2, F111–F122, doi: 10.1190/1.3549642.

Walsh, D. O., 2008, Multi-channel surface NMR instrumentation and software for 1D/2D groundwater investigations: Journal of Applied Geophysics, **66**, 140–150, doi: 10.1016/j.jappgeo.2008.03.006.